Journal of Manufacturing Processes 87 (2023) 133–140

Contents lists available at ScienceDirect

Journal of Manufacturing Processes

journal homepage: www.elsevier.com/locate/manpro

Load-bearing capacity of hybrid riv-bonded aluminum-magnesium joints at quasi-static and cyclic loadings

Josef Domitner [a,*], Zahra Silvayeh [a], Jožef Predan [b], Peter Auer [a], Jennifer Stippich [a], Norbert Enzinger [a], Nenad Gubeljak [b]

[a] Graz University of Technology, Institute of Materials Science, Joining and Forming, Research Group of Lightweight and Forming Technologies, Inffeldgasse 11/I, 8010 Graz, Austria

[b] University of Maribor, Faculty of Mechanical Engineering, Chair of Mechanics, Smetanova ulica 17, 2000 Maribor, Slovenia

ARTICLE INFO

Keywords:
Lightweight design
Car body manufacturing
Body-in-white
Aluminum alloy
Magnesium alloy
Riv-bonding
Adhesive
Self-piercing riveting
SPR
Static strength
Fatigue performance

ABSTRACT

The load-bearing capacity of hybrid riv-bonded aluminum-magnesium lap joints under shear-tensile loading was studied with particular focus on their static strength and fatigue performance. Sheets of 1.5 mm-thick EN AW-6016-T4 aluminum alloy were joined with sheets of 2 mm-thick AZ91 magnesium alloy using two high-strength steel rivets and epoxy-based adhesive. Local deformation-induced fracture of the comparatively inductile magnesium alloy sheet at the rivet holes during riveting at room temperature was intentionally tolerated. The lap joints were heat-treated to peak-age the aluminum alloy (condition T4 → T6) and to cure the adhesive between the sheets. Characteristic cross-section features and hardness maps were measured for assessing the quality of the joints and thus for proving the general capability of the riv-bonding process. The fracture behavior of the inductile magnesium alloy sheet determined the static strength as well as the fatigue performance at load ratios of 0.1 and 0.5. Both, load amplitude and mean load, influenced the site of fatigue crack initiation and the path of crack propagation. Local fracture of the inductile magnesium alloy sheet at the rivet hole is tolerable, if riv-bonded lap joints are just exposed to cyclic loading with low amplitudes.

1. Introduction

Substitution of conventional mild steels with materials of higher strength-to-weight ratio, such as advanced high-strength steels, light metal alloys and composite materials, can significantly decrease the vehicle weight, increase the fuel efficiency and, thus, reduce CO_2 emissions during service [1,2]. In particular, aluminum alloys [3,4] and magnesium alloys [5–7] are of interest for multi-material design of lightweight car bodies. However, dissimilar solid state and fusion welding [8], as well as mechanical joining [9,10] of these alloys are challenging, as aluminum and magnesium possess different thermo-physical properties, brittle intermetallic phases may form at elevated temperature, and magnesium has poor formability at room temperature. Nevertheless, integrating hybrid aluminum-magnesium (Al-Mg) components into car bodies-in-white (BIW) requires capable and cost-efficient joining technologies. In this respect the combination of self-piercing riveting (SPR) [11,12] and adhesive bonding [13,14], so-called riv-bonding, has emerged as the key technology for joining dissimilar materials in the automotive series production.

Riv-bonding processes, which include (i) applying the viscous adhesive onto the sheet surface, (ii) stacking the sheets, (iii) clamping the stack, and finally (iv) pushing the rivet into the stack (i.e., setting the rivet), are usually conducted at room temperature where the formability of most magnesium alloys is quite poor. Preheating magnesium alloy sheets to about 200 °C prior rivet setting, e.g., using a laser beam [15], an electric heating plate [16], or an induction coil [17], as well as simultaneous heating of the magnesium alloy sheets during rivet setting by, e.g., its own electric resistance [18], may improve the formability and thus reduce local cracking. Improved formability of magnesium alloy sheets is also achieved in friction self-piercing riveting (F-SPR), where frictional heat is generated by high-speed rotation of the rivet against the sheets during setting [19–24]. However, as additional technological measures obviously complicate the joining process and increase the overall process costs, their use in automotive series production has yet been limited. Hence, measures should be avoided if they are not absolutely necessary for achieving reliable joints.

* Corresponding author.
E-mail address: josef.domitner@tugraz.at (J. Domitner).

https://doi.org/10.1016/j.jmapro.2023.01.019
Received 1 September 2022; Received in revised form 24 December 2022; Accepted 10 January 2023
Available online 18 January 2023

Evaluating characteristic features of joint cross-sections (height of the rivet head, horizontal undercut of the rivet and minimum bottom thickness of the lower sheet) is a common practice for assessing the general quality and for analyzing the influence of different process parameters on the integrity of SPR joints of similar and dissimilar metals [25–29]. Moreover, characteristic features are often used for validating the results of numerical simulations of SPR processes [30–35] and of riv-bonding processes [45,47,48]. The detailed evaluation of cross-sections of Al-Mg joints enables identifying crack formation and local fracture, which may typically occur in the inductile magnesium alloy sheet next to the rivet [23,36,37], in particular, if the sheet is placed on the die side. Not only the cross-sections, but also strain hardening and residual stresses which are due to plastic deformation of the components during the SPR process influence the mechanical performance of Al-Mg joints [38–40].

Even though research activities on dissimilar mechanical joining of aluminum alloys with magnesium alloys have mainly focused on simple SPR joints, hybrid riv-bonded joints are of greater practical importance in the automotive industry. However, only a few studies investigated the influence of the adhesive on the riv-bonding process of similar steel joints [41–43], similar aluminum alloy joints [44–47], and dissimilar aluminum-steel joints [48]. The adhesive layer must be considered in the riveting process, as local cracking of the sheets may occur, if the adhesive layer becomes too thick and if large volumes of viscous adhesive must be displaced during the riveting process. The riv-bonding process, the static strength, the energy absorption and the fatigue performance of the joints are considerably influenced by the adhesive layer [49].

Compared to SPR joints, riv-bonded joints possess significantly better mechanical performance under quasi-static and cyclic loadings. This was demonstrated for similar joints of 0.8 mm-thick AM50 magnesium alloy sheets [50], as well as for similar joints of 2 mm-thick AA-5754-H32 [51], 2 mm-thick AA-6111-T4 [52] and 1.5 mm-thick EN AW-6016-T6 [53] aluminum alloy sheets. Moreover, the influence of the adhesive layer was studied for dissimilar joints of 2 mm-thick AA-5182-O aluminum alloy sheet with 1 mm-thick HSLA350 or 1.6 mm-thick DP600 high-strength steel sheet, respectively [54], and for dissimilar joints of 2.5 mm-thick AA-5052 aluminum alloy sheet with 1.5 mm-thick DC52D low-alloyed steel sheet [55]. However, to the author's knowledge detailed studies on the riv-bonding process and on the load-bearing capacities of dissimilar riv-bonded joints of ductile aluminum alloys and inductile magnesium alloys are lacking.

Fretting wear between the sheets caused by relative movement during cyclic testing was identified as the key mechanism that initiates fatigue cracking during cyclic loading of simple SPR joints of EN AW-6016-T6 aluminum alloy [53], AA-5754 aluminum alloy [56,57], AA-5052 aluminum alloy [58], AA-6111-T4 aluminum alloy with HSLA340 steel [59,60], and AA-6082 aluminum alloy with AM60 magnesium alloy [39,61]. However, the mechanism of fatigue cracking of hybrid riv-bonded joints is different, as the adhesive layer prevents direct fretting contact between the sheets and retards crack propagation [51–53]. In general, the adhesive layer determines the load-bearing properties, but the actual fracture mode of a specific joint configuration (fracture of the joint vs. fracture of the sheet) strongly depends on the particular loading conditions including load amplitude and mean load applied during cyclic testing [53,59,60].

Even though the manufacturing process, the static strength and the fatigue performance of simple self-piercing-riveted Al-Mg joints have basically been studied, fundamental knowledge about hybrid riv-bonded Al-Mg joints is still lacking. In particular, the influence of production-related defects (e.g., of surface cracks) requires deeper understanding. Therefore, the present work investigates the load-bearing capacity of riv-bonded joints of ductile 1.5 mm-thick commercial EN AW-6016-T4 aluminum alloy sheet and comparatively inductile 2 mm-thick commercial AZ91 magnesium alloy sheet under both quasi-static and cyclic shear-tensile loadings. This joint configuration can be used in car bodies, e.g., for joining an outer deep-drawn body panel (Al alloy) with a thicker inner reinforcement panel (Mg alloy) of higher strength.

2. Materials and methods

2.1. Material specifications

Sheets with dimensions of 100 mm × 90 mm were shear-cut from commercial 1.5 mm-thick EN AW-6016-T4 aluminum alloy which is typically used for producing outer-skin panels of car bodies, and from commercial 2 mm-thick rolled and annealed AZ91 magnesium alloy using a hydraulic guillotine. The aluminum alloy sheet was ¼ thinner than the magnesium alloy sheet. The side edges of each sheet were milled after cutting, since the condition of the side-edges of the magnesium alloy sheet was identified as critical with respect to the fracture behavior under cyclic loading [37]. The sheets were riv-bonded using two commercial Tucker C5.3×6.0-H4 (C-type semi-tubular rivet of hardness class H4 with diameter of 5.3 mm and height of 6.0 mm) manganese-boron steel rivets [62] and about 1 g of SikaPower®-498/3 single-component epoxy-based adhesive [63].

2.2. Riv-bonding process

A heating lamp was used for warming the viscous adhesive, which was stored in a cartridge, to the application temperature of 50–60 °C as recommended by the supplier. Before the AZ91 sheet was stacked with the EN AW-6016-T4 sheet, about 1 g of the adhesive was deposited on the joint area (90 mm × 20 mm) by using a manual cartridge gun. Manual compression and pre-fixation of the Al-sheet/adhesive/Mg-sheet stack using mechanical clamps distributed the adhesive between the sheets, and portions of the adhesive were even squeezed out of the joining gap. The overall thickness of the deposited adhesive layer was about 0.1–0.2 mm, but applying the blankholder force prior setting the rivets displaced the adhesive from the contact zone of the blankholder. Thus, the thickness of the adhesive layer decreased next to the rivets, but it increased at the center of the joint. The variation of the layer thickness due to the inhomogeneous distribution of the adhesive is characteristic for riv-bonded joints [44].

A manual Tucker riveting system including a massive C-frame, an ERC control unit, an electrically driven ERT80 spindle and a T031 flat pip die [62] were used for setting the rivets at room temperature. To reduce the cracking tendency, the comparatively inductile AZ91 sheet was placed on the punch side (upper sheet) and the EN AW-6016-T4 sheet was placed on the die side (lower sheet). Velocity and stroke of the riveting punch were 100 mm/s and 9.5 ± 0.1 mm, respectively, and the blankholder force applied for clamping the Al-sheet/adhesive/Mg-sheet stack was 8 kN. Table 1 provides a summary of the parameters of the riv-bonding process.

As illustrated in Fig. 1, total length, total width and overlapping length of each riv-bonded sample were 180 mm, 90 mm and 20 mm, respectively [37]. The distance between the rivet axes was 45 mm. The nominal cross-sections exposed to tensile loading were 180 mm^2 and 135 mm^2 for the AZ91 sheet and for the EN AW-6016 sheet, respectively. A spacing strip with 30 mm × 90 mm × 1.5/2.0 mm was finally glued onto the backside of each sheet to ensure that the tensile load could be applied in-plane with the adhesive layer. For comparing the static

Table 1
Parameters of the riv-bonding process.

Parameter	Value
Velocity of riveting punch	100 mm/s
Stroke of riveting punch	9.5 ± 0.1 mm
Blankholder force	8 kN
Overall thickness of adhesive layer	0.1–0.2 mm
Application temperature of adhesive	50–60 °C

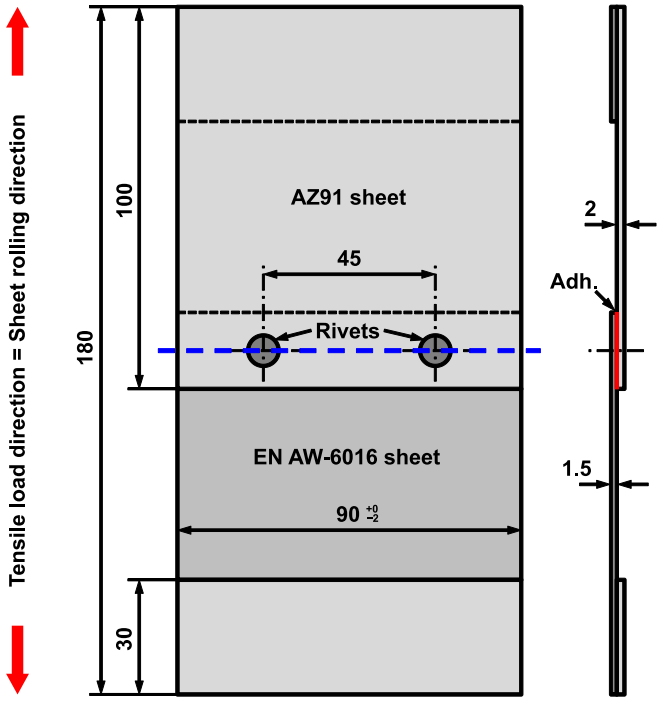

Fig. 1. Dimensions of riv-bonded samples. (For interpretation of the references to color in this figure, the reader is referred to the web version of this article.)

strengths of hybrid riv-bonded and simple SPR joints, three samples without adhesive were additionally prepared.

2.3. Heat treatment

After joining and before tensile testing, the joints were heat-treated for 20 min at 180–200 °C to cure the adhesive and to peak-age the aluminum alloy sheet. This heat treatment simulates the cathodic dip coating (CDC) process which is usually applied to car bodies-in-white (BIW) [53]. The stress-strain curves in Fig. 2 illustrate, that both yield strength and ultimate tensile strength of the EN AW-6016 alloy

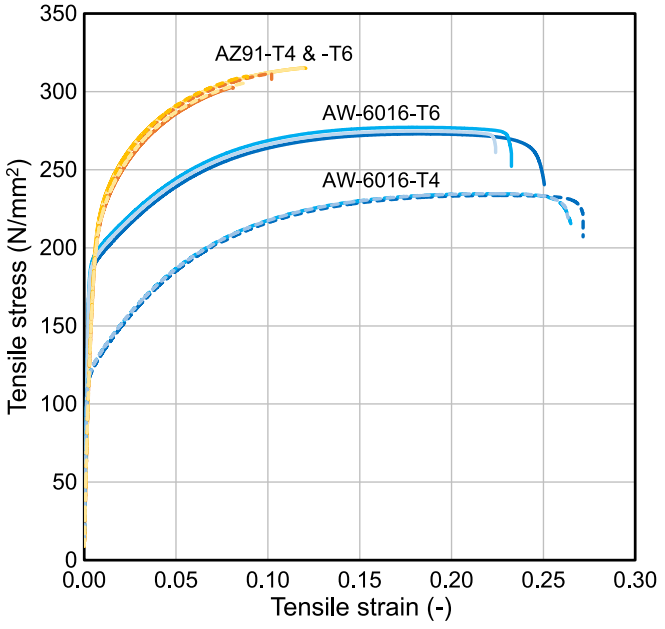

Fig. 2. Engineering stress-strain curves of EN AW-6016 and AZ91 before (T4) and after (T6) heat treatment.

increased but the ductility decreased in the peak-aged condition T6 after heat-treating compared to the as-delivered condition T4 before heat-treating. In contrast, tensile strength and ductility of the AZ91 alloy were almost identical before and after heat treatment. Yield strength, ultimate tensile strength and strain to fracture determined after heat treatment by quasi-static uniaxial tensile testing were 189 MPa, 275 MPa and 23 % for EN AW-6016-T6, and 200 MPa, 311 MPa and 10 % for AZ91, respectively [37]. The tensile strength of AZ91 was notably higher than the tensile strength of EN AW-6016-T6; however, the strain to fracture was less than half which confirms the poor ductility and formability of AZ91.

2.4. Quality assessment

The quality of the riv-bonded joints was assessed on the basis of characteristic cross-section features including height of the rivet head, horizontal undercut (interlock) of the rivet and minimum bottom thickness of the lower sheet. For that purpose the joints were sectioned as marked with the blue dashed line in Fig. 1 and embedded into epoxy resin. The cross-sections of the joints were ground, polished and finally captured using a Keyence VHX-6000 digital microscope. The topographies of the fracture surfaces after testing were captured using a Keyence VHX-7100 digital microscope equipped with a VHX-E500 objective lens for high-resolution three-dimensional imaging. Moreover, hardness maps for visualizing strain hardening of the sheets due to plastic deformation during rivet setting were captured at the cross-sections using an automated EMCO-TEST DuraScan G5 hardness tester. The distance between the HV0.05 hardness imprints in x- and y-direction was 0.1 mm. The Matlab software package was used for processing the measured data and for visualizing the hardness map.

2.5. Mechanical testing

A mechanical spindle-driven Zwick/Roell Z100 testing machine equipped with a 100 kN-load cell was used for quasi-static testing, whereas a servo-hydraulic Instron 1255 testing machine equipped with a 250 kN-load cell was used for cyclic testing. The 250 kN-load cell was calibrated particularly within the range of 10–100 kN to improve the measurement accuracy at low and medium loads. According to this calibration the relative measurement error was 0.55 % (55 N) at the load of 10 kN and 0.12 % (120 N) at the load of 100 kN. Quasi-static testing was performed with the constant speed of 5 mm/min. As proposed in [53], sinusoidal cyclic loading was applied with frequencies of 2 Hz at the low-cycle fatigue regime and 10 Hz at the high-cycle fatigue regime with load ratios of $R = 0.1$ and $R = 0.5$, respectively. R is the ratio between the cyclic load minimum, F_{min}, and the cyclic load maximum, F_{max}. Positive load ratios (i.e., $R > 0$) indicate that the samples were permanently under tension during cyclic testing. In each of the tests the number of cycles to failure of the sample was monitored. If the sample did not fail even though > 3 million cycles had been reached, cyclic testing was stopped. The highest load level which did not cause fracture/failure was considered as fatigue limit.

3. Results and discussion

3.1. Joint quality

Fig. 3(a) shows the representative cross-section of a riv-bonded sample after heat treatment, i.e., after the adhesive had been cured. The thickness of the adhesive layer between the upper magnesium alloy sheet and the lower aluminum alloy sheet was non-uniform. At the middle of the joint the local thickness was about 0.2–0.3 mm, which is moderately thicker than the initial layer thickness. Fig. 3(b) provides a more detailed view on the cross-section of the hybrid joint. It is evident that cavities filled with adhesive formed during the riveting process between the sheets next to the rivet. Moreover, a virtually adhesive-free

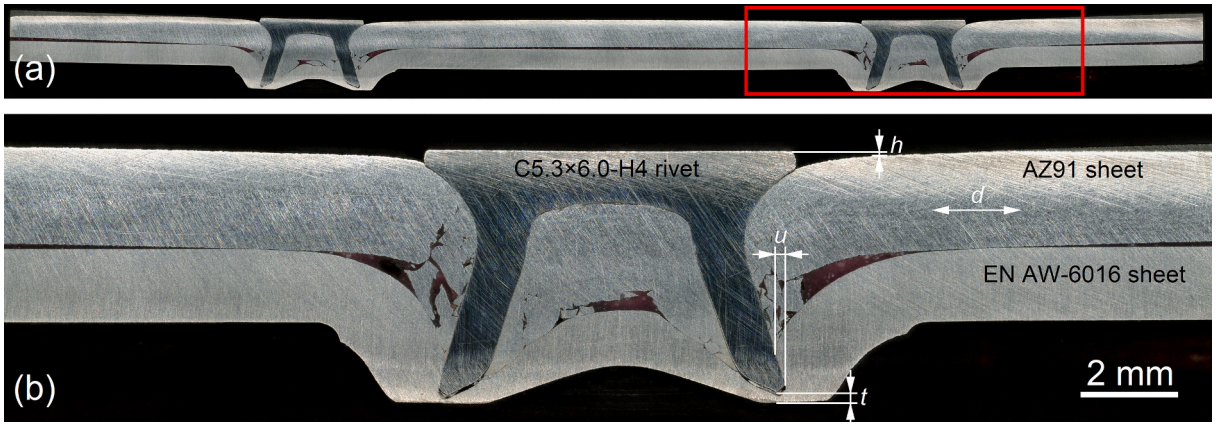

Fig. 3. (a) Typical cross-section of a riv-bonded sample, and (b) detailed view on the cross-section of a riv-bonded joint.

zone of $d \approx 2$ mm occurred, since applying the blankholder displaced the adhesive from this circular zone. Horizontal undercut (interlock) of the rivet, u, and minimum bottom thickness of the lower sheet, t, were both sufficient, and the height of the rivet head, h, was almost flush with the upper edge of the AZ91 sheet.

However, the low ductility of the magnesium alloy caused local fracture of the pierced upper sheet next to the rivet shaft during rivet setting. In contrast, cracking did not occur at the closing head of the joint next to the rivet tip, since the aluminum alloy sheet was more ductile. Even though local fracture of the upper sheet could not be avoided during riveting at room temperature, sufficient horizontal undercut of the rivet in the lower sheet ensures safe mechanical interlocking. As the riv-bonded joints had good dimensional quality, any possible scattering in their static strength and fatigue performance was obviously not related to any quality issues.

Fig. 4 illustrates the hardness map captured at the cross-section of a representative riv-bonded joint after heat-treatment. In general, the upper magnesium alloy sheet was softer than the lower aluminum alloy sheet, although the tensile strength and the ductility of both alloys, Fig. 2, would indicate an opposite tendency. Therefore, estimating the formability of dissimilar sheets just based on hardness measurements would be misleading, as low hardness is usually associated with higher ductility and better formability.

Severe plastic deformation during rivet setting caused strain hardening and local fracture of the upper AZ91 sheet next to the rivet shaft. However, strain hardening without any macroscopic fracture was observed at the lower EN AW-6016-T6 sheet next to the rivet tip at the closing head of the joint. The hardness of the heat-treated and peak-aged EN AW-6016-T6 sheet was about 90 HV0.05 at some distance to the rivet and about 110 HV0.05 at the severely deformed closing head of the joint. These hardness values are in good agreement with values reported for similar riv-bonded joints of identical sheets [53]. The AZ91 sheet showed comparatively low hardness of about 70 HV0.05 at some distance to the rivet, although notable local hardening of the sheet was observed next to the rivet shaft. Since deformation-induced strain hardening influences the material properties, the actual deformation history must be considered for predicting the static strength and/or the fatigue performance, as demonstrated for Al-Al [31,32] and Al-Mg [39] SPR joints. Hence, plastic deformations at joining spots should also be considered in the analysis of the fracture behavior of riv-bonded joints.

3.2. *Quasi-static load-bearing capacity of joints (static strength)*

Fig. 5(a) shows the force-displacement curves monitored during quasi-static shear-tensile testing of riv-bonded and of self-piercing-riveted Al-Mg lap joints (red continuous curves). For comparison, the diagram also includes the force-displacement curves of similar Al-Al lap joints (grey dashed curves, [53]). The dimensions of the Al-Mg and Al-Al joints were basically identical; however, one has to consider that the upper AZ91 sheet of the Al-Mg joint was 2 mm-thick, whereas the upper EN AW-6016-T6 sheet of the Al-Al joint was only 1.5 mm-thick. Even though the adhesive was identical for both types of joints, rivets of different length and hardness were used to ensure stable piercing of the different upper sheets and sufficient interlock between the rivet and the identical 1.5 mm-thick lower sheet.

Al-Mg joints were generally less stiff than Al-Al joints, as the initial

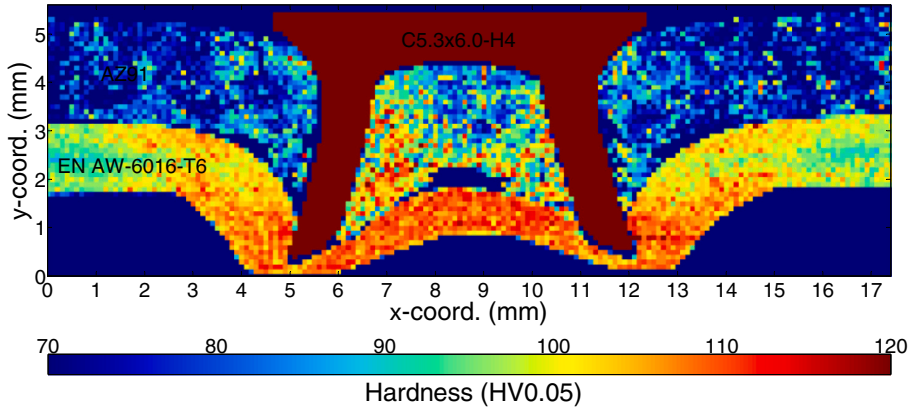

Fig. 4. Hardness map captured at the cross-section of a riv-bonded Al-Mg joint, which indicates strain hardening related to plastic deformation of the sheets. Each pixel represents one hardness imprint. The hardness of the embedding resin was ≪ 70 HV0.05 (dark blue areas) and the hardness of the rivet was ≫ 120 HV0.05 (dark red area). (For interpretation of the references to color in this figure legend, the reader is referred to the web version of this article.)

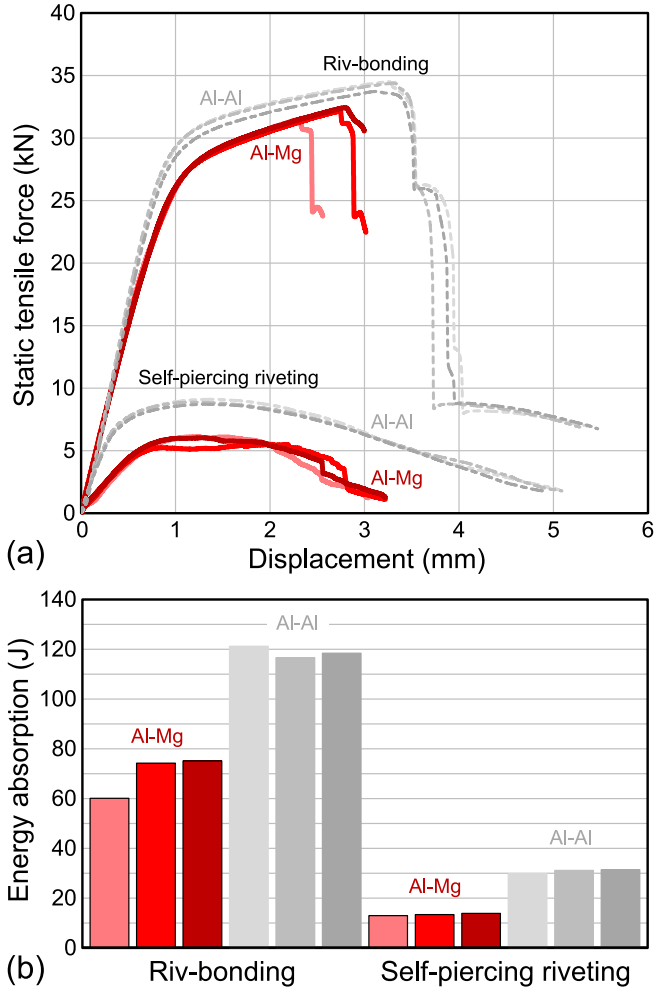

Fig. 5. Comparison of (a) force-displacement curves and (b) energy absorption determined in quasi-static testing of riv-bonded and self-piercing-riveted Al-Mg and Al-Al [53] lap joints.

slope of their force-displacement curves is notably flatter. Fracture of each joint was initiated at the tensile force maximum. The force maxima of riv-bonded and self-piercing-riveted Al-Mg joints of about 32 kN and 6 kN, respectively, were generally lower than the force maxima of the corresponding Al-Al joints of about 34 kN and 9 kN, respectively. The ratio of about ¼ between the force maxima of self-piercing-riveted and riv-bonded joints indicates, that the adhesive layer provided the main contribution to the total load-bearing capacity of the joints, whereas the rivets contributed just little. Previous studies confirmed this characteristic behavior [49–51,53,55]. In general, Al-Mg joints showed lower force maxima than Al-Al joints, but also less displacement to final fracture, which occurred for both types of joints when the rivets were rotated/pulled out from the lower sheet.

The lower force maximum and the lower displacement to final fracture reduce the energy absorbed by each of the joints. Fig. 5(b) compares the energy absorption of riv-bonded and self-piercing-riveted Al-Mg and Al-Al joints. The energy absorbed during quasi-static shear-tensile testing was calculated by numerical integration of the area below each of the curves shown in Fig. 5(a). In general, the energy absorption of self-piercing-riveted joints was about 70–80 % lower than the energy absorption of riv-bonded joints. The average energy absorption of riv-bonded and self-piercing-riveted Al-Mg joints was about 70 J and 13.5 J, respectively, which was significantly lower than the average energy absorption of Al-Al joints of about 119 J and 31 J, respectively. The main reason for the difference in the energy absorption of Al-Mg and Al-Al joints was the limited ductility of the AZ91 magnesium alloy which promoted crack initiation and propagation. This confirms the comparatively low strain to fracture of about 10 %, as shown in Fig. 2.

3.3. Cyclic load-bearing capacity of joints (fatigue performance)

The results of the cyclic tests are summarized in the logarithmic Woehler diagram [64] shown in Fig. 6, which correlates the load amplitude applied during cyclic testing, F_{amp}, with the number of cycles, N, counted until fracture of the joint occurred. Since the scattering of the markers is quite low, the applied riv-bonding process can be regarded as reliable. Markers showing large scattering because of poor joint preparation (e.g., samples with notches on the side edges of the magnesium alloy sheet [37] or with incomplete adhesive layer [53]) were intentionally excluded from the diagram. In general, N increased with decreasing F_{amp}. Moreover, N was notably higher for $R = 0.1$ (brown circular markers) than for $R = 0.5$ (orange square markers). Hence, the fatigue performance of Al-Mg joints increased not only with decreasing load amplitude, F_{amp}, but also with decreasing mean load, F_{mean}, as indicated by the decrease of the load ratio from $R = 0.5$ to 0.1. Within the medium- and high-cycle fatigue regimes Al-Al joints showed generally superior fatigue performance compared to Al-Mg joints. Below $F_{amp} \approx 10$ kN for $R = 0.1$ and below $F_{amp} \approx 6$ kN for $R = 0.5$, Al-Al joints showed higher N than Al-Mg joints. This mainly resulted from the higher ductility of the aluminum alloy sheet in comparison to the magnesium alloy sheet, which reduced the propagation rate of fatigue cracks. However, Al-Mg joints showed better fatigue performance than Al-Al joints at the low-cycle fatigue regime.

The relationship between the mean load, F_{mean}, and the load amplitude, F_{amp}, at the fatigue limit is presented in the Haigh diagram [64] shown in Fig. 7. Measured values are marked with filled circles, whereas extrapolated values are marked with empty circles. Based on the average quasi-static force maximum at $R = 1$ ($F_{amp} = 0$) extracted from the curves displayed in Fig. 5(a), and based on the fatigue limit at $R = 0.1$ ($F_{amp} = 3.38$ kN) and at $R = 0.5$ ($F_{amp} = 3$ kN) marked with arrows in Fig. 6, the fatigue limit at $R = 0$ ($F_{amp} = 3.45$ kN $= F_{mean}$) and at $R = -1$ ($F_{amp} = 3.63$ kN, $F_{mean} = 0$) was estimated. This estimation, however, does not consider any excessive buckling of the thin sheets which may occur under compression loadings. As the grey curve is located above the red

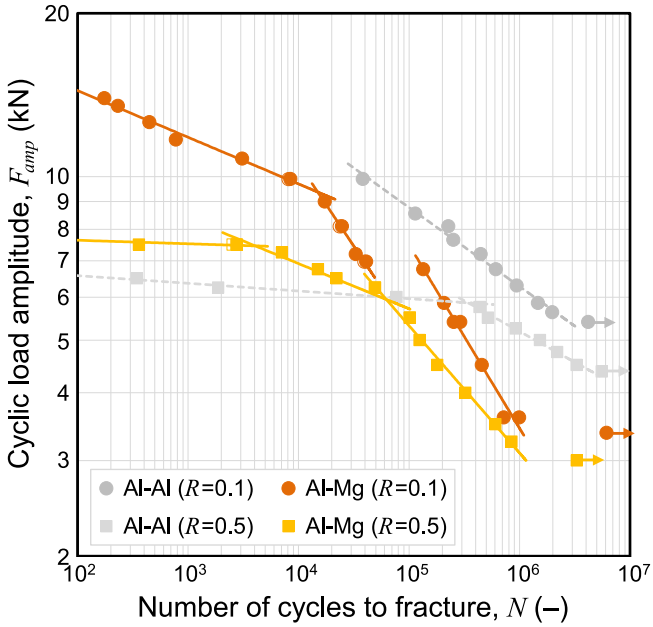

Fig. 6. Comparison of fatigue curves of riv-bonded Al-Mg and Al-Al [53] lap joints determined in cyclic testing at load ratios of $R = 0.1$ and $R = 0.5$.

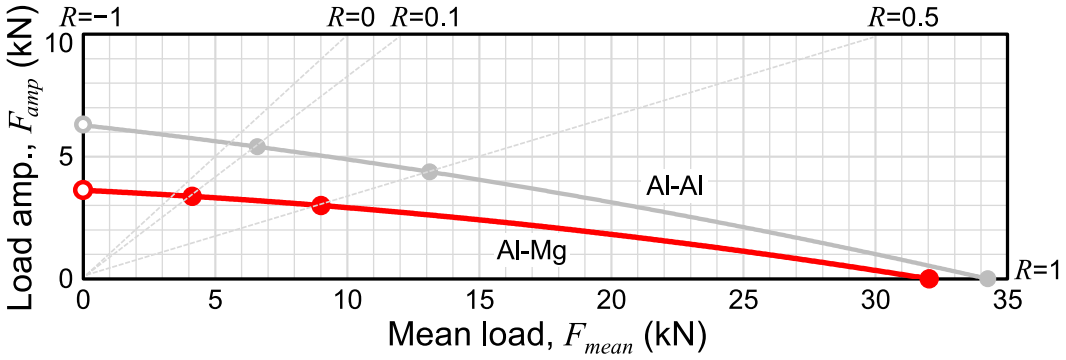

Fig. 7. Relationship between the mean load, F_{mean}, and the load amplitude, F_{amp}, at the fatigue limit for different load ratios, R, of Al-Mg joints (red curve) and of comparable Al-Al joints (grey curve). (For interpretation of the references to color in this figure legend, the reader is referred to the web version of this article.)

curve within the entire range of $R = -1$ to $R = 1$, the fatigue limit of Al-Mg lap joints can be generally considered as lower than the fatigue limit of comparable Al-Al lap joints.

The fatigue curves of the Al-Mg joints shown in Fig. 6 have two different slopes: the curves are comparatively flat within the low-cycle fatigue regime, i.e., for $F_{amp} > 9$ kN at $R = 0.1$ and for $F_{amp} > 6$ kN at $R = 0.5$, whereas the curves are much steeper within the medium- and high-cycle fatigue regimes, i.e., for $F_{amp} \approx 3.5$–9 kN at $R = 0.1$ and for $F_{amp} \approx 3$–6 kN at $R = 0.5$. The fatigue curve for $R = 0.1$ shows an offset at $F_{amp} \approx 7$ kN, which is not the case for the fatigue curve of the Al-Al joints. The different slopes as well as the offset of the fatigue curves are related to the fracture behavior of the samples, which strongly depends on the particular loading condition.

3.4. Fracture behavior

Fig. 8 compares the predominant fracture behavior of riv-bonded Al-Mg samples which had been exposed to (a) quasi-static and to (b-f) cyclic shear-tensile loadings at different F_{amp}, but at constant load ratio of $R = 0.1$. A recent study on the fracture behavior of self-piercing-riveted and riv-bonded Al-Al samples identified five different fracture modes: mode I is related to quasi-static loading, modes II and III are mainly related to cyclic loading of self-piercing-riveted joints, whereas modes IV and V are mainly related to cyclic loading of riv-bonded joints [53]. Because of the lower ductility of AZ91 compared to EN AW-6016-T6, similar – but not identical – fracture behavior as for Al-Al joints was observed for the Al-Mg joints in the present work.

At quasi-static loading fracture of the upper magnesium alloy sheet occurred directly at the joint. As shown in Fig. 8(a) the crack propagated through both rivet holes (mode IV). After cohesive failure of the adhesive layer, fracture of the inductile upper magnesium alloy sheet was initiated perpendicular to the load direction more or less simultaneously at both pre-cracked rivet holes. Failure without any fracture of the upper sheet just by rotating/pulling out both rivets from the lower aluminum alloy sheet as proposed for Al-Al joints (mode I) did not occur for Al-Mg joints.

At the low-cycle fatigue regime, i.e., at high F_{amp} where the fatigue curve is comparatively flat, fracture also occurred directly at the joint. The low-cycle fatigue fracture behavior was almost identical to the quasi-static fracture behavior, since the fatigue crack was initiated at the rivet holes. As illustrated in Fig. 8(b), final fracture of the joint occurred at the upper magnesium alloy sheet after failure of the adhesive layer (mode IV). Moreover, one of the rivets was additionally rotated/pulled out from the lower aluminum alloy sheet at a few samples, as demonstrated in Fig. 8(c). However, completely different fracture behavior was observed at the medium- and high-cycle fatigue regimes, i.e., at medium and low F_{amp} where the fatigue curve is steeper.

At $F_{amp} \approx 7$ kN the fatigue curve for $R = 0.1$ shows an offset which can be explained by the different fracture behavior of the samples. At $F_{amp} \approx 7$–9 kN fracture of the upper magnesium alloy sheet occurred exclusively next to the joint (mode V), as shown in Fig. 8(d). At $F_{amp} \approx 3.5$–7 kN fatigue fracture was initiated at only one of both rivet holes, but the crack propagated through the magnesium alloy sheet, as illustrated in Fig. 8(e). As the adhesive layer was able to retard the propagation of fatigue cracks, N was higher for fracture initiation at the rivet hole directly at the joint, than for fracture initiation at the magnesium

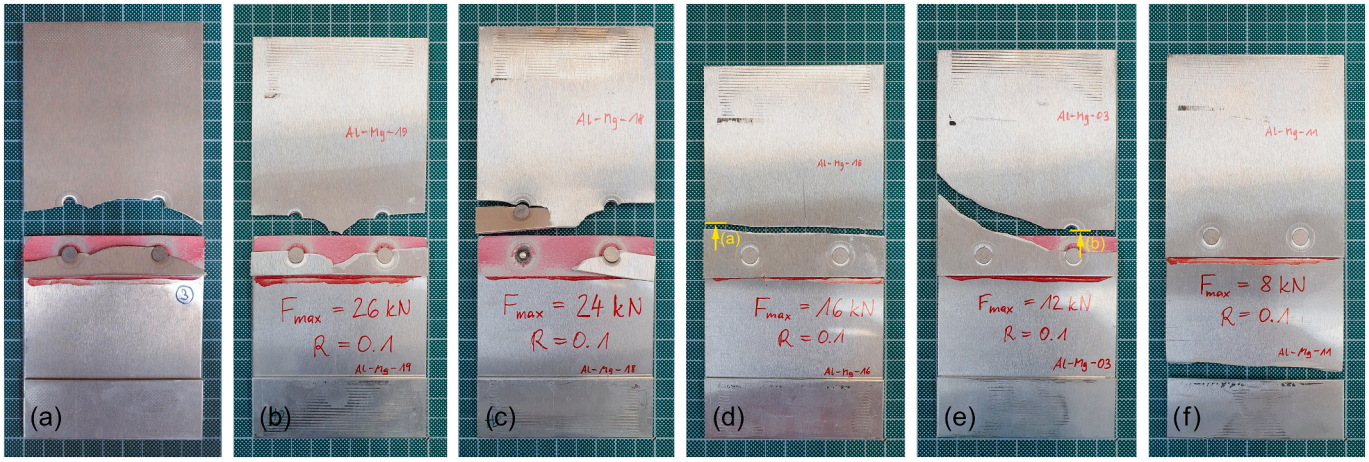

Fig. 8. Predominant fracture behavior of samples in (a) quasi-static and (b–f) cyclic shear-tensile testing at $R = 0.1$. From left to right the number of cycles to fracture, N, increases and the load amplitude, F_{amp}, decreases. The yellow arrows mark the positions of the detailed fracture surfaces shown in Fig. 9. (For interpretation of the references to color in this figure legend, the reader is referred to the web version of this article.)

alloy sheet next to the joint. At $F_{amp} \approx 3.5$ kN the aluminum alloy sheet failed next to the clamp of the testing machine (mode V), as shown in Fig. 8(f). This indicates that at low F_{amp} the aluminum alloy sheet was more sensitive to local stress concentrations than the magnesium alloy sheet. Fracture of the sheets next to the rivets (modes II and III, as typically observed for SPR joints) did not occur, since the adhesive layer prevented fretting.

At $R = 0.1$ fracture was either located at the joint or at one of both sheets; however, at $R = 0.5$ fracture was only located at the joint, but not at any of the sheets. Therefore, the fatigue curve shown in Fig. 7 for $R = 0.5$ does not show any offset. Moreover, this confirms that the actual fracture behavior does not depend only on the applied load amplitude, F_{amp}, but also on the applied mean load, F_{mean}, as expressed by the load ratio, R. Fig. 8 demonstrates that quasi-static strength and low-cycle fatigue performance are mainly determined by the properties of the riv-bonded joint which are influenced by the capability of the joining process (a–c), but the medium- and high-cycle fatigue performance is rather determined by the properties of the sheets (d–f). This trend was also observed in fatigue testing of riv-bonded Al-Al joints [53].

Fig. 9 shows details of two fracture surfaces with different sites of fatigue crack initiation, which significantly influenced the actual fracture behavior of the magnesium alloy sheet. Fig. 9(a) illustrates crack initiation on the surface of the magnesium alloy sheet (red oval). The semi-elliptical zone of slow stable crack propagation (smooth fracture surface enclosed by the dashed yellow line) is well distinguishable from the zone of fast crack propagation (rough fracture surface beyond the dashed yellow line). For comparison, Fig. 9(b) illustrates crack initiation at one of the rivet holes directly at the joint (red oval). As the adhesive layer between the magnesium alloy sheet and the aluminum alloy sheet retarded crack propagation during cyclic loading, the zone of slow stable crack propagation is considerably larger, and the zone of fast crack propagation is even not visible.

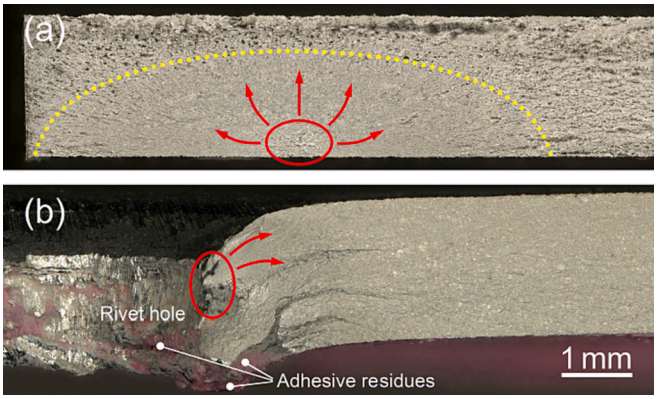

Fig. 9. Details of the fracture surfaces of two samples showing fatigue crack initiation (a) on the surface of the magnesium alloy sheet and (b) at the rivet hole of the magnesium alloy sheet. The viewing direction is parallel to the loading direction, as marked with the yellow arrows in Fig. 8.

4. Conclusions

The results of this experimental study led to the following conclusions, which are particularly valid if the inductile 2 mm-thick AZ91 magnesium alloy sheet is placed on the punch side (upper sheet) and the ductile 1.5 mm-thick EN AW-6016-T4/T6 aluminum alloy sheet is placed on the die side (lower sheet) of the joint:

(1) Riv-bonded lap joints of high dimensional quality were basically prepared. Interlock of the rivet and minimum bottom thickness of the lower EN AW-6016-T4 sheet were sufficient, and the rivet head was almost flush with the upper surface of the AZ91 sheet. However, local fracture at the rivet holes of the pierced AZ91 sheet occurred during riveting at room temperature.
(2) Tensile strength and thickness were notably higher for the AZ91 sheet than for the EN AW-6016-T6 sheet; however, the inductile AZ91 sheet affected both the static strength and the fatigue performance of the joints. The number of cycles to fracture decreased with increasing load amplitude or with increasing mean load as expressed by the load ratio, respectively.
(3) In cyclic testing the load amplitude and the mean load influenced both the initiation site of fatigue cracking and the path of crack propagation. In particular, the offset of the fatigue curve at the load ratio of 0.1 was related to the change of the fracture behavior at different load amplitudes.
(4) At quasi-static as well as at low-cycle fatigue loading (i.e., at high load amplitudes), fracture of the AZ91 sheet was initiated at both rivet holes and it occurred directly at the joint after failure of the adhesive. Thus, the quasi-static and the low-cycle fatigue performance, particularly at high load ratio, were mainly influenced by the actual quality of the joint, which is dependent on the capability of the riv-bonding process.
(5) At medium-cycle fatigue loading, fracture was initiated either at a single rivet hole or at the AZ91 sheet next to the joint. At high-cycle fatigue loading (i.e., at low load amplitudes close to the fatigue limit), fracture was even initiated at the EN AW-6016-T6 sheet. Thus, the medium- and high-cycle fatigue performance was mainly influenced by the properties of the sheets.
(6) Local deformation-induced cracking of the AZ91 sheet at the rivet holes is tolerable, if the riv-bonded Al-Mg lap joints are just exposed to cyclic loading with low amplitudes during service. Thus, additional technical measures aiming to increase the ductility of the AZ91 sheet during the riveting process are occasionally unnecessary.

Declaration of competing interest

The authors declare that they have no known competing financial interests or personal relationships that could have appeared to influence the work reported in this paper.

Acknowledgement

The authors would like to thank STANLEY® Engineered Fastening, Tucker GmbH, for providing the SPR system. Thanks go to Herbert Penker for assisting the quasi-static tests, and to Filip Jerenec, Luka Ferlič and Primož Štefane for assisting the cyclic tests.

Funding

Part of this study was co-funded by the Erasmus+ program of the European Union (EU) and by the program for Scientific & Technological Cooperation of the Austrian Federal Ministry of Education, Science and Research (BMBWF) and of the Slovenian Ministry of Education, Science and Sport (MESS). This joint program is managed by the Austrian Agency for Education and Internationalization (OeAD) and by the Slovenian Research Agency (ARRS). Open access funding was provided by Graz University of Technology.

References

[1] Taub AI, Luo AA. Advanced lightweight materials and manufacturing processes for automotive applications. MRS Bull 2015;40:1045–53.
[2] Taub A, De Moor E, Luo A, Matlock DK, Speer JG, Vaidya U. Materials for automotive lightweighting. Annu Rev Mat Res 2019;49:327–59.
[3] Miller WS, Zhuang L, Bottema J, Wittebrood AJ, De Smet P, Haszler A, Vieregge A. Recent development in aluminium alloys for the automotive industry. Mater Sci EngA 2000;280:37–49.
[4] Hirsch J. Recent development in aluminium for automotive applications. Trans Nonferrous Met Soc China 2014;24:1995–2002.

[5] Friedrich H, Schumann S. Research for a "new age of magnesium" in the automotive industry. J Mater Process Technol 2001;117:276–81.
[6] Easton M, Beer A, Barnett M, Davies C, Dunlop G, Durandet Y, Blacket S, Hilditch T, Beggs P. Magnesium alloy applications in automotive structures. JOM 2008;60:57–62.
[7] Kulekci MK. Magnesium and its alloys applications in automotive industry. Int J Adv Manuf Technol 2008;39:851–65.
[8] Liu L, Ren D, Liu F. A review of dissimilar welding techniques for magnesium alloys to aluminum alloys. Materials 2014;7:3735–57.
[9] Groche P, Wohletz S, Brenneis M, Pabst C, Resch F. Joining by forming – a review on joint mechanisms, applications and future trends. J Mater Process Technol 2014;214:1972–94.
[10] Meschut G, Merklein M, Brosius A, Drummer D, Fratini L, Füssel U, Gude M, Homberg W, Martins PAF, Bobbert M, Lechner M, Kupfer R, Gröger B, Han D, Kalich J, Kappe F, Kleffel T, Köhler D, Kuball C-M, Popp J, Römisch D, Troschitz J, Wischer C, Wituschek S, Wolf M. Review on mechanical joining by plastic deformation. J Adv Join Process 2022;5:100113.
[11] He X, Pearson I, Young K. Self-pierce riveting for sheet materials: state of the art. J Mater Process Technol 2008;199:27–36.
[12] Li D, Chrysanthou A, Patel I, Williams G. Self-piercing riveting – a review. Int J Adv Manuf Technol 2017;92:1777–824.
[13] Cavezza F, Boehm M, Terryn H, Hauffman T. A review on adhesively bonded aluminium joints in the automotive industry. Metals 2020;10:730.
[14] Maggiore S, Banea MD, Stagnaro P, Luciano G. A review of structural adhesive joints in hybrid joining processes. Polymers 2021;13:3961.
[15] Durandet Y, Deam R, Beer A, Song W, Blacket S. Laser assisted self-pierce riveting of AZ31 magnesium alloy strips. Mater Des 2010;31:S13–6.
[16] Wang JW, Liu ZX, Shang Y, Liu AL, Wang MX, Sun RN, Wang P-C. Self-piercing riveting of wrought magnesium AZ31 sheets. J Manuf Sci Eng 2011;133:031009.
[17] Stephens E, Soulami A, Nyberg E, Sun X, Ramasamy S, Kenyon B, Belknap R. SPR process simulation, analyses, and development for magnesium joints. In: DOE Vehicle Technologies Office 2014 Annual Merit Review, Washington, DC, June 16-20; 2014.
[18] Klein T, Kirov G, Ucsnik S. Self-piercing riveting of medium- and high-strength Al and mg alloy sheets enabled by in-process electric resistance heating. J Manuf Sci Eng 2021;143:034502.
[19] Li YB, Wei ZY, Wang ZZ, Li YT. Friction self-piercing riveting of aluminum alloy AA6061-T6 to magnesium alloy AZ31B. J Manuf Sci Eng 2013;135:061007.
[20] Ma Y, Lou M, Yang Z, Li Y. Effect of rivet hardness and geometrical features on friction self-piercing riveted joint quality. J Manuf Sci Eng 2015;137:054501.
[21] Liu X, Lim YC, Li Y, Tang W, Ma Y, Feng Z, Ni J. Effects of process parameters on friction self-piercing riveting of dissimilar materials. J Mater Process Technol 2016;237:19–30.
[22] Ma Y, He G, Lou M, Li Y, Lin Z. Effects of process parameters on crack inhibition and mechanical interlocking in friction self-piercing riveting of aluminum alloy and magnesium alloy. J Manuf Sci Eng 2018;140:101015.
[23] Ma Y, Niu S, Shan H, Li Y, Ma N. Impact of stack orientation on self-piercing riveted and friction self-piercing riveted aluminum alloy and magnesium alloy joints. Automot Innov 2020;3:242–9.
[24] Yang B, Ma Y, Shan H, Niu S, Li Y. Friction self-piercing riveting (F-SPR) of aluminum alloy to magnesium alloy using a flat die. J Magnes Alloys 2022;10:1207–19.
[25] Haque R. Quality of self-piercing riveting (SPR) joints from cross-sectional perspective: a review. Arch Civil Mech Eng 2018;18:83–93.
[26] Xu Y. Effects of factors on physical attributes of self-piercing riveted joints. Sci Technol Weld Join 2006;1(6):666–71.
[27] Li D. Influence of local surface texture by tool impression on the self-piercing riveting process and the static lap shear strength. J Manuf Process 2017;29:298–309.
[28] Karim MA, Jeong T-E, Noh W, Park K-Y, Kam D-H, Kim C, Nam D-G, Jung H, Park Y-D. Joint quality of self-piercing riveting (SPR) and mechanical behavior under the frictional effect of various rivet coatings. J Manuf Process 2020;58:466–77.
[29] Li M, Liu Z, Huang L, Chen Q, Tong C, Fang Y, Han W, Zhu P. Automatic identification framework of the geometric parameters on self-piercing riveting cross-section using deep learning. J Manuf Process 2022;83:427–37.
[30] Hönsch F, Domitner J, Sommitsch C, Götzinger B, Kölz M. Numerical simulation and experimental validation of self-piercing riveting (SPR) of 6xxx aluminium alloys for automotive applications. J Phys Conf Ser 2018;1063:012081.
[31] Hönsch F, Domitner J, Sommitsch C, Götzinger B. Modeling the failure behavior of self-piercing riveting joints of 6xxx aluminum alloy. J Mater Eng Perform 2020;29:4888–97.
[32] Rusia A, Weihe S. Development of an end-to-end simulation process chain for prediction of self-piercing riveting joint geometry and strength. J Manuf Process 2020;57:519–32.
[33] Du Z, Duan L, Jing L, Cheng A, He Z. Numerical simulation and parametric study on self-piercing riveting process of aluminium-steel hybrid sheets. Thin-Walled Struct 2021;164:107872.
[34] Karathanasopoulos N, Pandya KS, Mohr D. An experimental and numerical investigation of the role of rivet and die design on the self-piercing riveting joint characteristics of aluminum and steel sheets. J Manuf Process 2021;69:290–302.
[35] Zhao H, Han L, Liu Y, Liu X. Analysis of joint formation mechanisms for self-piercing riveting (SPR) process with varying joining parameters. J Manuf Process 2022;73:668–85.
[36] Luo A, Lee T, Carter J. Self-pierce riveting of magnesium to aluminum alloys. SAE Int J Mater Manuf 2011;4(1):158–65.
[37] Domitner J, Silvayeh Z, Predan J, Jerenec F, Auer P, Stippich J, Ferlič L, Štefane P, Sommitsch C, Gubeljak N. Influence of the sheet edge condition on the fracture behavior of riv-bonded aluminum-magnesium joints. Key Eng Mater 2022;926:1541–8.
[38] Moraes JFC, Jordon JB, Su X, Brewer LN, Fay BJ, Bunn JR, Sochalski-Kolbus L, Barkey ME. Residual stresses and plastic deformation in self-pierce riveting of dissimilar aluminum-to-magnesium alloys. SAE Int J Mater Manuf 2018;11(2):139–49.
[39] Moraes JFC, Jordon JB, Su X, Barkey ME, Jiang C, Ilieva E. Effect of process deformation history on mechanical performance of AM60B to AA6082 self-pierce riveted joints. Eng Frac Mech 2019;209:92–104.
[40] Lee Y-I, Kim H-K. Effects of residual stresses on the fatigue lifetimes of self-piercing riveted joints of AZ31 Mg alloy and Al5052 Al alloy sheets. Metals 2021;11:2037.
[41] Fricke H, Israel M. Simulation von Hybridfügeprozessen – Unterschiedliche Werkstoffe prozesssicher verbinden. Adhäsion 2011;55(7–8):24–9.
[42] Neugebauer R, Israel M, Mayer B, Fricke H. Numerical and experimental studies on the clinch-bonding and Riv-bonding process. Key Eng Mater 2012;504–506:771–6.
[43] Fricke H, Vallée T. Numerical modeling of hybrid-bonded joints. J Adhes 2016;92:652–64.
[44] Landgrebe D, Mayer B, Niese S, Fricke H, Neumann I, Ahnert M, Falk T. Adhesive distribution and global deformation between hybrid joints. Key Eng Mater 2015;651–653:1465–71.
[45] Potgorschek L, Domitner J, Hönsch F, Sommitsch C, Kaufmann S. Numerical simulation of hybrid joining processes: self-piercing riveting combined with adhesive bonding. Procedia Manuf 2020;47:413–8.
[46] Liu Y, Han L, Zhao H, Liu X. Experimental investigation of the adhesive layer's impact on the Riv-bonding process and joint quality. Thin-Walled Struct 2021;167:108255.
[47] Liu Y, Han L, Zhao H, Liu X. Numerical modelling and experimental investigation of the riv-bonding process. J Mater Process Technol 2021;288:116914.
[48] Domitner J, Auer P, Stippich J, Silvayeh Z, Jessernig S, Peiser L, Hönsch F, Sommitsch C. Riv-bonding of aluminum alloys with high-strength steels against the favorable joining direction. J Mater Eng Perform 2022;31(9):6970–9.
[49] Moroni F, Pirondi A, Kleiner F. Experimental analysis and comparison of the strength of simple and hybrid structural joints. Int J Adhes Adhes 2010;30:367–79.
[50] Miyashita Y, Jack Teow YC, Karasawa T, Aoyagi N, Otsuka Y, Mutoh Y. Strength of adhesive aided SPR joint for AM50 magnesium alloy sheets. Procedia Eng 2011;10:2532–7.
[51] Moroni F. Fatigue behaviour of hybrid clinch-bonded and self-piercing rivet bonded joints. J Adhes 2019;95(5–7):577–94.
[52] Wu G, Li D, Lai W-J, Shi Y, Kang H, Peng Y, Su X. Fatigue behaviors and mechanism-based life evaluation on SPR-bonded aluminum joint. Int J Fatigue 2021;142:105948.
[53] Domitner J, Silvayeh Z, Predan J, Auer P, Stippich J, Sommitsch C, et al. Load-bearing capacities and fracture modes of self-piercing-riveted, adhesive-bonded and riv-bonded aluminum joints at quasi-static and cyclic loadings. J Mater Eng Perform 2022. https://doi.org/10.1007/s11665-022-07677-5.
[54] Sun X, Stephens EV, Khaleel MA. Fatigue behaviors of self-piercing rivets joining similar and dissimilar sheet metals. Int J Fatigue 2007;29:370–86.
[55] Jiang H, Liao Y, Gao S, Li G, Cui J. Comparative study on joining quality of electromagnetic driven self-piecing riveting, adhesive and hybrid joints for Al/steel structure. Thin-Walled Struct 2021;164:107903.
[56] Chen YK, Han L, Chrysanthou A, O'Sullivan JM. Fretting wear in self-piercing riveted aluminium alloy sheet. Wear 2003;255:1463–70.
[57] Iyer K, Hu SJ, Brittman FL, Wang PC, Hayden DB, Marin SP. Fatigue of single- and double-rivet self-piercing riveted lap joints. Fatigue Fract Eng Mater Struct 2005;28:997–1007.
[58] Zhao L, He X, Xing B, Lu Y, Gu F, Ball A. Influence of sheet thickness on fatigue behavior and fretting of self-piercing riveted joints in aluminum alloy 5052. Mater Des 2015;87:1010–7.
[59] Huang L, Bonnen J, Lasecki J, Guo H, Su X. Fatigue and fretting of mixed metal self-piercing riveted joint. Int J Fatigue 2016;83:230–9.
[60] Huang L, Shi Y, Guo H, Su X. Fatigue behavior and life prediction of self-piercing riveted joint. Int J Fatigue 2016;88:96–110.
[61] Kang H-T, Boorgu S. Fatigue life prediction of self-piercing rivet joints between magnesium and aluminum alloys. MATEC Web Conf 2018;165:10004.
[62] STANLEY® Engineered Fastening Tucker GmbH. Self piercing rivet catalog and die overview T-numbers. 2017. Gießen, Germany.
[63] Sika Automotive GmbH. Product Data Sheet SikaPower®-498/3 Crash resistant metal adhesive. 2016. Hamburg, Germany.
[64] Haibach E. Betriebsfestigkeit – Verfahren und Daten zur Bauteilberechnung. 3rd Edition. Berlin-Heidelberg, Germany: Springer; 2006.